



1 Merging TEMPEST Microwave and GOES-16 Geostationary IR soundings for 2 improved water vapor profiles

3

4 Chia-Pang Kuo¹, Christian Kummerow¹

5 ¹Department of Atmospheric Science, Colorado State University, Fort Collins, CO 80523, USA

6

7 Correspondence to: Chia-Pang Kuo (chia-pang.kuo@colostate.edu)

8

9 **Abstract.** The Temporal Experiment for Storms and Tropical Systems Demonstration (TEMPEST-D)
10 demonstrated the capability of CubeSat satellites to provide high-quality, stable microwave signals for
11 estimating water vapor, clouds, and precipitation from space. Unlike the operational NOAA and MetOp
12 series satellites, which combine microwave and hyperspectral infrared sensors on the same platforms
13 to optimize retrievals, CubeSat radiometers such as TEMPEST do not carry additional sensors. In such
14 cases, the high temporal and spatial resolution and multi-channel measurements from the Advanced
15 Baseline Imager (ABI) on the next-generation series of Geostationary Operational Environmental
16 Satellites (GOES-R) are ideal for assisting these smaller, stand-alone radiometers. Based on sensitivity
17 tests, the water vapor retrievals from TEMPEST are improved by adding water-vapor-sounding
18 channels at 6.2, 6.9, and 7.3 mm from ABI, which help to increase the vertical resolution of soundings
19 and reduce retrieval errors. Under clear sky conditions, retrieval biases and root-mean-square errors
20 improve by approximately 10 %, while under cloudy skies, biases remain unchanged but root-mean-
21 square errors still decrease by 5 %. Humidity soundings are also validated using coastal radiosonde
22 data from the Integrated Global Radiosonde Archive (IGRA) from 2019 to 2020. When ABI indicates
23 clear skies, water vapor retrievals improve somewhat by decreasing the overall bias in the microwave
24 only estimate by roughly 10 %, although layer root-mean-square errors remain roughly unchanged at 1
25 g/kg when three ABI channels are added. When ABI indicates cloudy conditions, there is little change in
26 the results. The small number of matched radiosondes may limit the observed improvement.

27

28 1. Introduction

29

30 The Temporal Experiment for Storms and Tropical Systems Demonstration (TEMPEST-D; Reising et al.,
31 2018) mission was designed to demonstrate the capability of a small radiometer on board a 6U
32 CubeSat satellite for deriving clouds, water vapor, and precipitation. The CubeSat, including the flight
33 system and the TEMPEST-D radiometer, is 10 cm x 20 cm x 34 cm and weighs 11.2 kg. Although the size
34 of the TEMPEST-D is much smaller than instruments such as the operational Microwave Humidity
35 Sounders (MHS on NOAA-18/19 and MetOp-A/B/C), which weigh about 63 kg, the TEMPEST-D
36 radiometer demonstrated the capability to provide comparable well-calibrated microwave (MW)
37 measurements (Berg et al., 2021; Brown et al., 2023). In addition, Schulte et al. (2020) introduced the
38 bias correction of Earth incidence angle (EIA) (Schulte and Kummerow, 2019) in the Optimal Estimation
39 (OE; Rodgers, 2000) framework with TEMPEST-D and demonstrated the potential of getting consistent
40 retrievals from a fleet of TEMPEST sensors observing the same spot with different EIAs. Radhakrishnan
41 et al. (2022) estimated surface rainfall by machine-learning methods and showed that retrieved rainfall
42 using TEMPEST-D channels was consistent with the multi-radar/multi-sensor system (MRMS) rainfall
43 products over the Continental United States. The success of TEMPEST-D led to flying a second TEMPEST



44 unit in conjunction with the Compact Ocean Wind Vector Radiometer (COWVR;
45 <https://podaac.jpl.nasa.gov/COWVR-TEMPEST>) currently in orbit aboard the International Space
46 Station.

47
48 Several studies have shown the capability of retrieving surface and atmospheric variables over the
49 ocean under non-raining conditions using Optimal Estimation (OE) techniques. Elsaesser and
50 Kummerow (2008) retrieved total precipitable water (TPW), surface wind, and cloud liquid water path
51 (CLWP) using observations from the Advanced Microwave Scanning Radiometer-Earth Observing
52 System (AMSR-E), the Special Sensor Microwave/Imager (SSM/I), and the Tropical Rainfall Measuring
53 Mission (TRMM) Microwave Imager (TMI) using the same OE configurations. This was later expanded
54 to the Global Precipitation Measurement (GPM) Microwave Imager (GMI) (Duncan and Kummerow,
55 2016). The Colorado State University 1 D variational inversion algorithm (CSU 1DVAR) has been
56 validated by comparing results with other independent products, showing that CSU 1DVAR can provide
57 consistent results across a broad spectrum of sensors (Elsaesser and Kummerow, 2008; Duncan and
58 Kummerow, 2016; Schulte and Kummerow, 2019; Schulte et al., 2020). A conceptually similar OE
59 method is employed in the Microwave Integrated Retrieval System (MiRS; Boukabara et al., 2011,
60 2013, 2018) designed to provide various atmospheric and surface parameters (skin temperature,
61 surface emissivity, and profiles of temperature, water vapor, non-precipitating clouds, and
62 precipitations) under all sky conditions over ocean and land surfaces. Due to its flexible structure, MiRS
63 is used operationally at NOAA and supports measurements from multiple MW instruments, including
64 the TMI, GMI, MHS, Atmospheric Microwave Sounding Unit (AMSU), SSM/I, Special Sensor Microwave
65 Imager/Sounder (SSM/I), and Advanced Technology Microwave Sounder (ATMS).

66
67 Infrared (IR) sounders and especially hyperspectral IR sounders, while limited to clear sky conditions,
68 have distinct advantages for deriving temperature and moisture profiles due to their sharper weighting
69 functions, particularly in the upper troposphere when no clouds are present. Using MW measurements
70 from AMSU-A and MHS plus IR observations from the Improved Atmospheric Sounding in the Infrared
71 (IASI) on board the MetOp platforms, Aires (2011) and Aires et al. (2011, 2012) significantly reduced
72 the errors of retrieving temperature and water vapor profiles under clear sky conditions over the
73 ocean by comparing with retrievals using individual MW or IR instruments alone. Under the European
74 Space Agency Water Vapour Climate Change Initiative project (Siddans et al., 2015; Siddans, 2019),
75 Trent et al. (2023) validated 9.5 years of atmospheric profiles retrieved from MetOp MW and IR
76 observations and showed that global biases of temperature and water vapor are within 0.5 K and 10 %,
77 respectively, making the retrieval products an important climate data record.

78
79 In addition to MW and IR measurements on the MetOp platforms, Milstein and Blackwell (2016) also
80 showed the advantages of using MW and IR spectral bands from the Atmospheric Infrared Sounder
81 (AIRS) and AMSU on the Aqua satellite as well as from the Cross-Track Infrared Sounder (CrIS) and
82 ATMS on the Suomi National Polar-orbiting Partnership satellite (Suomi NPP) for temperature and
83 water vapor retrievals. The NOAA Unique CrIS/ATMS Processing System (NUCAPS; Gambacorta et al.,
84 2012) was built specifically to retrieve global atmospheric profiles using MW sensors (ATMS, AMSU,
85 and MHS) and hyperspectral IR instruments (CrIS or AIRS) under non-precipitating conditions with up
86 to 80 % effective cloud fraction. Sun et al. (2017) used radiosonde data to assess the sounding products
87 from NUCAPS, indicating small biases in the lower atmosphere for temperature profiles of less than 0.5



88 K and less than 20 % for water vapor profiles. These profiles have been further improved by Ma et al.
89 (2021), who applied a neural network technique to enhance the retrieved atmospheric profiles in
90 NUCAPS products by using IR channels on the next-generation series of Geostationary Operational
91 Environmental Satellites (GOES-R; Schmit et al., 2008). The root-mean-square error of retrieved
92 temperature and humidity profiles in that study decreased by more than 30 % from the surface up to
93 700 hPa. Thus, while it seems clear from these previous studies that merging IR and MW soundings
94 from the same platforms is beneficial, CubeSat sounders such as TEMPEST or the Time-Resolved
95 Observations of Precipitation structure and storm Intensity with a Constellation of Smallsats (TROPICS;
96 Blackwell et al., 2018) do not generally fly in tandem with hyperspectral IR sounders. In this case, it is
97 useful to examine if there are benefits to merging the stand-alone passive MW sensors with
98 geostationary IR-sounding channels.

99

100 The Advanced Baseline Imager (ABI), on board the GOES-R satellite series, observes the full disk of the
101 Earth every 10 minutes (15 minutes prior to April 2019), measuring in the visible (VIS), near-IR, and IR
102 spectral bands with spatial resolutions from 0.5 to 2 km. Three water vapor channels at (6.2, 6.9, and
103 7.3 mm) make ABI suitable for deriving water vapor profiles with similar vertical resolution to the
104 operational MW sensors (Schmit et al., 2008; Li et al., 2019). Due to the high spatial and temporal
105 resolutions from GOES-R ABI observations over large regions, the ABI sensor can always be matched
106 with stand-alone MW radiometers over the sensed hemisphere, as illustrated by Ma et al. (2021). This
107 study thus focuses on the enhancement in water vapor retrievals that may be achieved when ABI IR
108 water vapor sounding channels are added to the TEMPEST-D MW channels.

109

110 2. Data

111

112 The TEMPEST-D satellite (Reising et al., 2018) was deployed from the International Space Station on
113 July 13, 2018, into the Low Earth Orbit. The initial orbit height was 400 km with a 51.6° inclination,
114 observing an 825 km wide swath from the initial height. The mission successfully demonstrated both
115 the maneuverability of CubeSats to fly in closely maintained formations, as well as the calibration
116 stability of the MW radiometer (Berg et al., 2021). The TEMPEST-D passive MW radiometer scanned
117 Earth in a cross-track mode and measured five channels at 87, 164, 174, 178, and 181 GHz with quasi-
118 horizontal polarization, except for 87 GHz, which measured quasi-vertical polarization. The spatial
119 resolutions of TEMPEST-D at the nadir were 14 km at 164 to 181 GHz and 28 km at 87 GHz. While the
120 data is not complete due to difficulties with the data receiving station at Wallops Island, Virginia, USA,
121 all available TEMPEST-D datasets can be requested through the website <https://tempest.colostate.edu>.
122 TEMPEST-D was deorbited on June 22, 2021. A second copy of TEMPEST was launched on Dec. 21,
123 2021, and is operating on the International Space Station in conjunction with COWVR. Data is available
124 from the National Aeronautics and Space Administration (NASA) Physical Oceanography Distributed
125 Active Archive Center (PODAAC) housed at NASA's Jet Propulsion Laboratory. Because the instruments
126 and orbits are identical, the results presented here apply to both sensors.

127

128 The GOES-16 (Schmit et al., 2008; Li et al., 2019) is the first of the GOES-R series satellites and was
129 launched on November 19, 2016, carrying several instruments, including ABI. GOES-16 replaces GOES-
130 13 and is located at longitude 75.2°W in a geostationary orbit (35786 km altitude), observing from
131 latitude 81.32°N to 81.32°S and from longitude 156.30°W to 6.30°E. This covers North and South



132 America, the eastern Pacific Ocean, and the Atlantic Ocean to the west coast of Africa. The ABI sensor
133 measures 16 spectral channels from VIS to IR bands (0.47 to 13.3 μm) with spatial resolutions ranging
134 from 0.5 km at 0.64 μm to 2.0 km in the IR. In this study, three ABI-sounding channels at 6.2, 6.9, and
135 7.3 μm are used to enhance the TEMPEST-D retrieved water vapor profiles. To ensure spatial
136 consistency between TEMPEST-D and the GOES-16, ABI full disk products, all Radiances (RadF), Clear
137 Sky Masks (ACMF), Cloud Top Phase (ACTPF), and Cloud Top Pressure (CTPF) products from ABI, are
138 averaged to match the 28 km TEMPEST-D horizontal resolution and appended to TEMPEST-D
139 observation locations and times. The GOES-16 products can be downloaded through the
140 Comprehensive Large Array Data Stewardship System (CLASS). Although GOES-17 also covers parts of
141 the TEMPEST-D operational period, its products are not used to avoid all issues related to the cooling
142 system, as described in <https://www.goes-r.gov/users/GOES-17-ABI-Performance.html>.

143
144 Except for satellite observations and products mentioned above, auxiliary data, including surface wind
145 speed and direction, surface pressure, surface skin temperature, and temperature profiles, are also
146 used to constrain the retrievals. These are taken from the ERA5 (Hersbach et al., 2020), accessed
147 through the website <https://www.ecmwf.int/en/forecasts/dataset/ecmwf-reanalysis-v5>. The hourly
148 ERA5 data used in the study are $0.5^\circ \times 0.5^\circ$ with 27 pressure levels from 1000 to 100 hPa. The vertical
149 resolution (in pressure coordinates) consists of 25 hPa intervals from 1000 to 750 hPa, 50 hPa intervals
150 from 750 to 250 hPa, and 25 hPa intervals from 250 to 100 hPa. One hour temporal resolution and 0.5°
151 spatial resolution from ERA5 is used to define unobserved surface conditions as well as the
152 temperature profiles. Since five TEMPEST-D and three ABI-sounding channels are more sensitive to
153 water vapor, retrievals are not particularly sensitive to the variability in ancillary parameters.
154 Therefore, the auxiliary surface parameters and temperature profiles are linearly interpolated in space
155 and time to match the TEMPEST-D observations.

157 3. Methods

158
159 In satellite remote sensing, OE is a widely utilized technique to retrieve atmospheric components
160 (Rodgers, 2000; Elsaesser and Kummerow, 2008; Boukabara et al., 2011; Siddans et al., 2015; Duncan
161 and Kummerow, 2016; Schulte and Kummerow, 2019; Schulte et al., 2020). In OE, the state parameters
162 and measurement errors are all assumed to follow a Gaussian distribution, and the atmospheric states
163 being retrieved, x , are optimally estimated by minimizing the cost function J ,

$$165 J = (x - x_a)^T S_a^{-1} (x - x_a) + [y - f(x)]^T S_y^{-1} [y - f(x)], \quad (1)$$

166
167 where x_a is the a priori information about the state vector x , y is the measurement vector, $f(x)$ is a
168 forward model simulating measurements for a given state x , S_a is the covariance matrix of a priori, and
169 S_y is the covariance matrix of measurement errors (Rodgers, 2000). The minimization of J is achieved
170 by iteratively solving for the state vector x using the Gauss-Newton method. Following Eq. 5.29 in
171 Rodgers (2000), the convergence criteria are achieved when

$$173 d_i^2 = (x_i - x_{i+1})^T \hat{S}^{-1} (x_i - x_{i+1}) \ll n, \quad (2)$$

174



175 where d measures the change in the state vector between i th and i th + 1 iteration, and n is the
 176 number of retrieved variables (levels of water vapor and/or layers of clouds in this study). The solution
 177 is said to have converged when the residual is one tenth the number of the retrieved variables in the
 178 study. This is consistent with the definition from Eq. (2) that the error weighted increment is much less
 179 than the number of the retrieved variables. The a priori state vector x_a is used as the initial guess at
 180 the beginning of the iteration. The a priori information x_a and its uncertainty S_a are derived from
 181 monthly ERA5 humidity and cloud profiles over the ocean; x_a describes the mean state of the profiles,
 182 and S_a accounts for the variation of the states.

183
 184 The state vector x comprises the water vapor mixing ratio at different pressure levels and/or clouds.
 185 The number of selected water vapor levels depends on the number of channels and the assumptions of
 186 clouds. The selected water vapor levels are evenly distributed in pressure levels at 1000, 900, 800, 600,
 187 and 400 hPa for TEMPEST only, and 1000, 950, 875, 800, 700, 600, 450, and 350 hPa when both
 188 TEMPEST and ABI channels are used. The remaining water vapor levels are linearly interpolated.
 189 Following previous studies (Schulte and Kummerow, 2019; Schulte et al., 2020), clouds are inserted
 190 into single layers containing liquid and/or ice clouds in the profiles. If clouds are assumed to be
 191 present, the state vector will contain one layer of liquid and one layer of ice clouds with liquid cloud
 192 top at 900 hPa and ice cloud top at 300 hPa. If cloud information is derived from GOES-16 products,
 193 liquid clouds and/or ice clouds can also be inserted following GOES-16 cloud information as listed in
 194 Table 1.

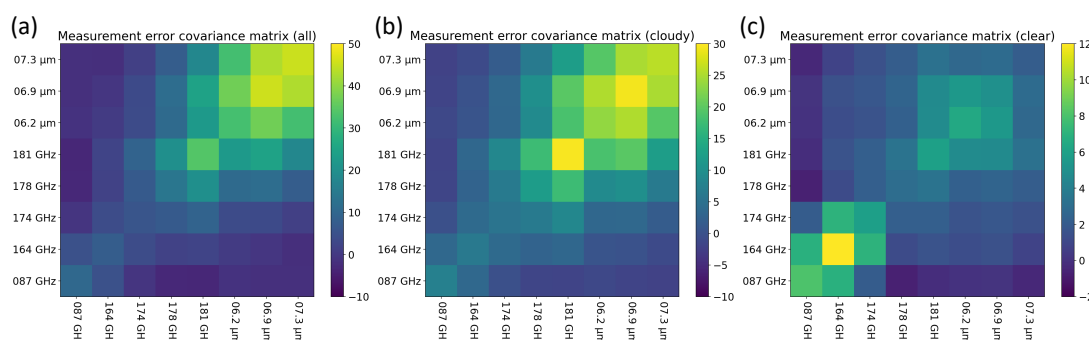
195
 196
 197 Table 1. The retrieval configurations under clear and cloudy conditions with and without GOES-16
 198 cloud information. CF, CH, and CP represent cloud fraction, cloud height, and cloud phase, respectively.
 199

Sensors	Using GOES-16 cloud products	
	Clear sky	Cloudy sky
TEMPEST+ABI (8 channels) or TEMPEST (5 channels)	1. No, set CF to 1 2. Yes, set CF to 0	1. No, set CF to 1 2. Yes, set CF from GOES-16 3. Yes, set CF, CH, and CP from GOES-16

200
 201
 202 The measurement error covariance matrix S_y is derived from two uncertainty sources: the radiometer
 203 and the forward model (Elsaesser and Kummerow, 2008; Duncan and Kummerow, 2016; Schulte and
 204 Kummerow, 2019; Schulte et al., 2020). The noise equivalent differential temperature (NEDT) values
 205 are represented as the radiometer measurement errors for each sensor channel. For TEMPEST, the
 206 NEDT values are 0.20, 0.35, 0.55, 0.55, and 0.75 K, respectively, for 87 to 181 GHz (Berg et al., 2021),
 207 and 0.1 K for all ABI IR channels, except for band 16, which is 0.3 K (Goodman et al., 2019). The forward
 208 model uncertainties are approximated by comparing simulated satellite observations using full ERA5
 209 profiles to degraded simulated measurements using the assumptions made in the OE retrievals, as
 210 described above. While the radiative transfer model is assumed to contain no errors, errors are
 211 introduced when complex water vapor profiles are replaced by simplified water vapor profiles at the
 212 prescribed levels, and complex cloud vertical profiles are replaced by single liquid and ice cloud layers



213 containing the equivalent cloud water path. The measurement error covariance matrix S_y is then
214 derived from the NEDT values and the estimated forward model errors. Figures 1(a), 1(b), and 1(c)
215 show the S_y estimated from all, cloudy, and clear skies, respectively, based on oceanic ERA5 profiles.
216 Since ERA5 profiles most often contain some degree of clouds, Figs. 1(a) and 1(b) have similar patterns,
217 and channels having similar water vapor sensitivity are more correlated with each other. On the other
218 hand, due to much lower atmospheric absorption in the clear skies, the surface-sensitive TEMPEST
219 channels (87 and 164 GHz) have higher correlations among themselves as in Fig. 1(c), although with
220 smaller overall S_y values than in Figs. 1(a) and 1(b).
221
222



223
224 Figure 1. Measurement error covariance matrix S_y for five TEMPEST-D MW and three ABI IR channels
225 derived from ERA5 profiles under (a) all sky, (b) cloudy sky, and (c) clear sky conditions over the ocean.
226
227

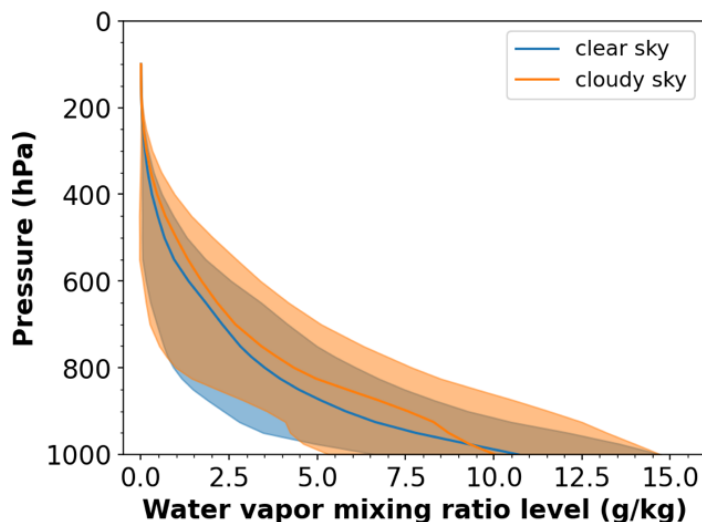
228 The forward model is composed of two radiative transfer models: one simulates MW observations, and
229 the other computes IR measurements. In the study, the Community Radiative Transfer Model (CRTM;
230 Liu et al., 2012; Johnson et al., 2023) version 2.3.0 is used to calculate the observed brightness
231 temperature for the ABI IR channels. The model can be downloaded through the website
232 <https://github.com/JCSDA/crtm>. To simulate TEMPEST MW observations, an Eddington approximation,
233 as described in Schulte and Kummerow (2019) and Schulte et al. (2020), is used. The Monochromatic
234 Radiative Transfer Model (MonoRTM; http://rtweb.aer.com/monortm_frame.html; Clough et al.,
235 2005) is used to generate the atmospheric absorption while the ocean surface MW emissivity is
236 computed using the FAST microwave Emissivity Model version 6 (FASTEM-6; Kazumori and English,
237 2015). Clouds are assumed to be homogeneously distributed in single layers. The cloud top pressure is
238 900 hPa for liquid clouds and 300 hPa for ice clouds if no cloud top heights are assigned from GOES-16
239 products, as described earlier. The MW optical properties of liquid clouds are generated by Lorenz-Mie
240 theory (van de Hulst, 1957; Bohren and Huffman, 1998), assuming the droplet is spherical with a radius
241 of 12 μm and is monodisperse in particle size distribution (PSD). The radiative properties of ice clouds
242 in the MW spectrum are computed using the single-scattering property databases for non-spherical ice
243 particles from Liu (2008) and Nowell et al. (2013) following the analysis of Schulte and Kummerow
244 (2019). The databases are derived by the discrete-dipole approximation method (Draine and Flatau,
245 1994). The microphysical properties of ice clouds used to derive the scattering properties are assumed
246 to have the PSD from Field et al. (2007) with a constant density of 100 g/cm^3 and have ice habits: 6



247 bullet rosettes (crystal size $< 800 \mu\text{m}$) and aggregates of $400 \mu\text{m}$ rosettes (crystal size $\geq 800 \mu\text{m}$). Ice
248 clouds can be one of the major error sources in radiative transfer simulations (Kulie et al., 2010;
249 Ringerud et al., 2019; Schulte and Kummerow, 2019), but are not considered here.

250
251 The monthly means and variability of water vapor mixing ratios from ERA5 above 200 hPa are
252 extremely small, as shown in Fig. 2. The sensor responses to these small amounts of stratospheric
253 water vapor are less than the noise of 0.2 to 0.75 K for TEMPEST and 0.1 to 0.3 K for ABI. Therefore,
254 the water vapor mixing ratio was set to the monthly mean climatology above 200 hPa and is not
255 retrieved explicitly with the available channels.

256
257



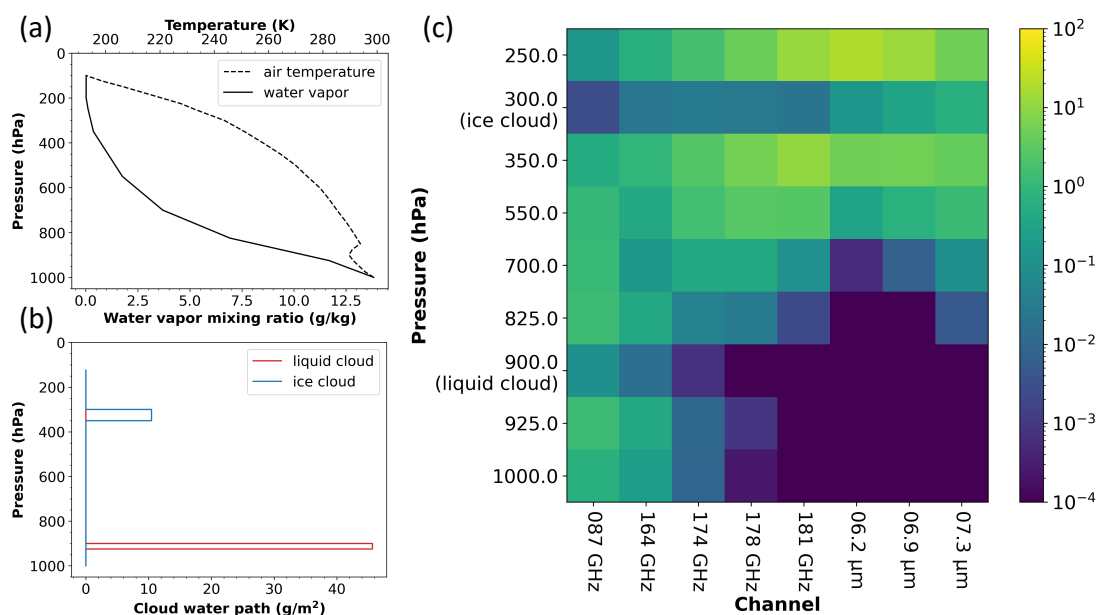
258
259 Figure 2. Monthly mean and standard deviation (σ) of water vapor profiles under clear and cloudy
260 conditions over the ocean between $\pm 60^\circ$ latitudes from ERA5 in May 2020. Blue color represents
261 water vapor in clear skies, while orange color shows water vapor in cloudy skies. Solid lines are mean
262 water vapor profiles, and shaded areas are standard deviations.

263
264

265 With the model configuration described above, and a priori atmospheric temperature and water vapor
266 profiles from ERA5 shown in Figs. 3(a) and 3(b), the sensitivity of water vapor and liquid and ice clouds
267 to five TEMPEST-D MW channels and three ABI IR bands is represented by the Jacobians shown in Fig.
268 3(c). For humidity, all TEMPEST MW and ABI IR channels have different degrees of sensitivity along the
269 altitude axis. In the presence of clouds, three ABI water-vapor-sounding channels only provide signals
270 for the upper atmosphere. However, under the same conditions, signals of water vapor are sensed by
271 the TEMPEST MW bands from the surface to the top of the atmosphere. TEMPEST 87 and 164 GHz
272 spectral bands have significant sensitivity to water vapor and liquid clouds through the entire lower
273 atmosphere. Except for the TEMPEST 87 GHz band, all remaining TEMPEST channels have sensitivity to
274 ice clouds. Overall, as also shown in the studies mentioned in the introduction (Aires, 2011; Milstein
275 and Blackwell, 2016; Sun et al., 2017; Ma et al., 2021; Trent et al., 2023), Fig. 3(c) demonstrates the

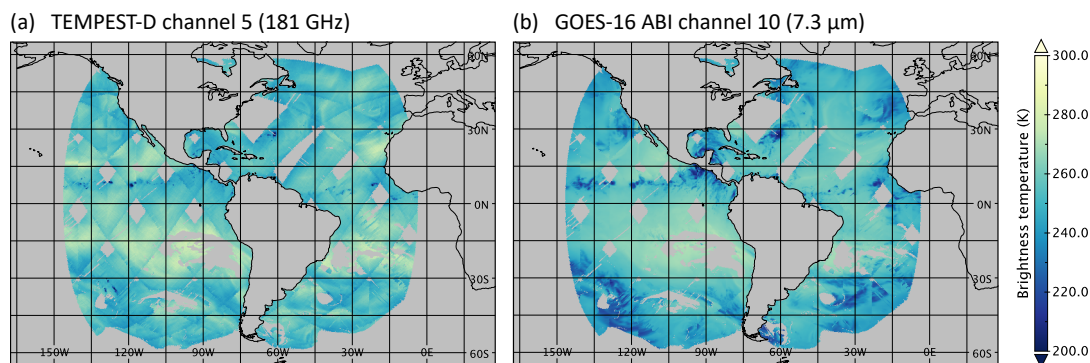


276 advantage of merging IR spectral and MW spectral bands in soundings: MW channels have humidity
277 signals under cloudy conditions, and IR bands provide extra information about the upper atmosphere.
278
279



280
281 Figure 3. An example of water vapor and cloud Jacobians and the ERA5 profiles over the ocean used to
282 compute the Jacobians. (a) Profiles of air temperature and water vapor mixing ratio. (b) Profiles of
283 liquid and ice clouds. (c) Water vapor Jacobians from 250 to 1000 hPa and Jacobians of liquid (cloud
284 top at 900 hPa) and ice (cloud top at 300 hPa) clouds as a function of sensor channels (TEMPEST-D
285 from 87 to 181 GHz and ABI from 6.2 to 7.3 μm). The unit of the color for water vapor Jacobians is
286 K/g/kg, and for liquid and ice cloud Jacobians is K/g/m².
287
288

289 Given the frequent observation from GOES-R ABI, the data can be readily merged with TEMPEST-D.
290 Figure 4 shows the overlap of the two sensors over the ocean. Gaps between MW orbits as well as
291 cloudy regions where ABI detects clouds are evident in both images. Even though ABI cannot be used
292 for sounding in cloudy atmospheres, using the ABI cloud products can still provide retrievals some prior
293 knowledge about clouds (cloud fraction, phase, and height), which will be shown to positively impact
294 the TEMPEST-D MW retrievals. The next section will explore retrieval sensitivities under clear and
295 cloudy conditions using synthetic TEMPEST-D and ABI observations simulated from ERA5 profiles.
296 Retrieved water vapor profiles are then validated against in situ radiosonde humidity measurements
297 under different retrieval assumptions, as listed in Table 1.
298
299



300 Figure 4. Collocated TEMPEST-D and GOES-16 ABI observations over the ocean on 2020/06/01 for (a)
301 TEMPEST-D channel 5 (181 GHz) and for (b) ABI channel 10 (7.3 μm).
302
303

304 4. Results

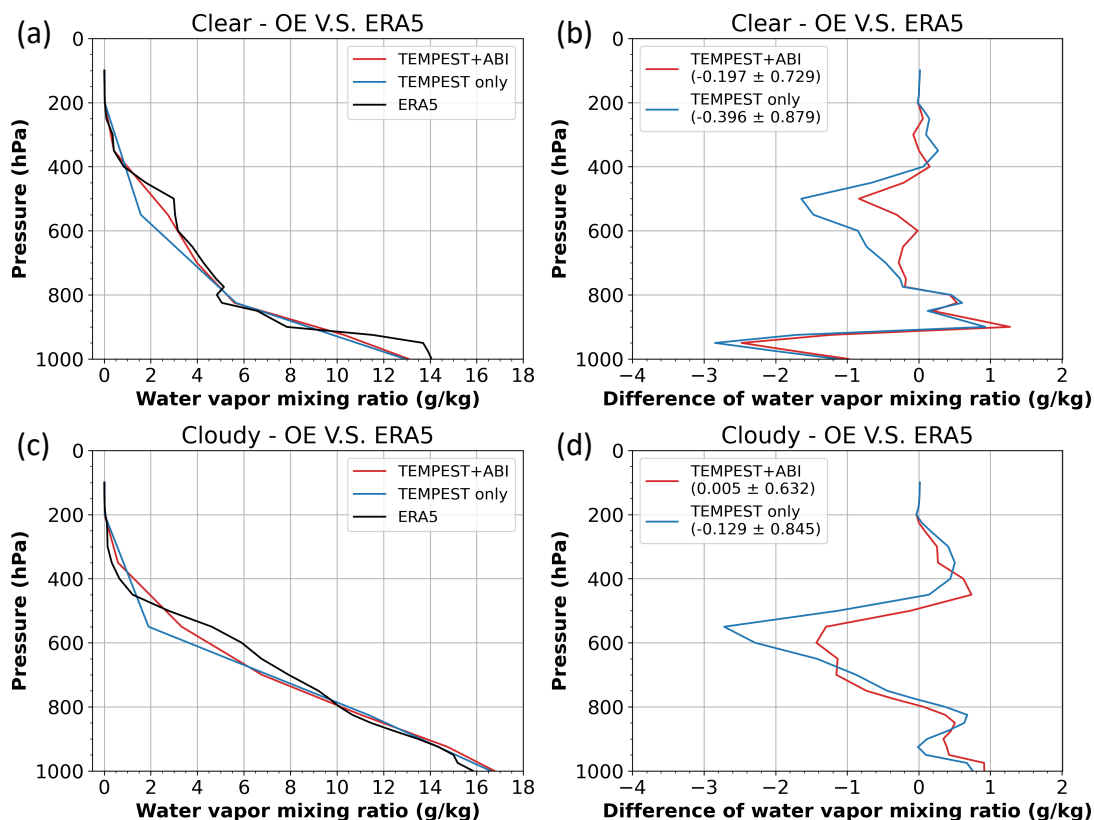
305 4.1. Sensitivity Tests

306
307
308 Observations for the TEMPEST five (87, 164, 174, 178, and 181 GHz) and ABI three (6.2, 6.9, and 7.3
309 μm) channels are simulated using temperature, humidity, cloud profiles, surface temperature, and
310 surface wind speed and direction from ERA5 over the ocean with viewing angles corresponding to
311 TEMPEST and ABI instruments respectively. All data corresponds to May 27, 2020. Since the true states
312 from the ERA5 data are known, the retrieval accuracy can be evaluated using the computed observed
313 brightness temperature under different scenarios.
314

315 4.1.1. Case studies

316
317 Two cases are used to illustrate the humidity retrievals first using only the TEMPEST sensor and then
318 adding three ABI channels in clear and cloudy sky scenes. These are shown in Fig. 5. While the
319 retrieved profiles do not change dramatically, the additional ABI water-vapor-sounding channels can
320 be seen to improve the mid-tropospheric biases and standard deviations, as shown in Figs. 5(b) and
321 5(d) respectively. Although the retrieved water vapor profiles are over- and under-estimated along the
322 height when compared to the true ERA5 values, Fig. 5 reveals that the retrievals using three extra ABI
323 IR channels improve significantly with respect to both bias and standard deviation above the 800 hPa
324 level where the ABI channels are expected to add the most information. While overall biases and
325 standard deviations also decrease for both examples, it is apparent that ABI has little influence over
326 the low-level water vapor, and that most of the improvement actually comes from the mid to upper
327 troposphere.
328

329
330



331
 332 Figure 5. Selected cases of retrieved water vapor profiles using the synthetic observations from ERA5
 333 over the ocean on 2020/05/27. Figures (a) and (b) show retrievals under clear conditions, while cloudy
 334 retrievals are presented in Figures (c) and (d). Figures (a) and (c) show the retrieved and ERA5 humidity
 335 profiles, and the corresponding comparisons between retrievals and ERA5 (retrievals minus ERA5)
 336 are presented in Figures (b) and (d). The solid black lines are water vapor profiles from ERA5. The solid red
 337 lines are water vapor retrievals using TEMPEST and ABI combined channels, and the solid blue lines are
 338 retrievals using the TEMPEST sensor. The number in the parentheses is the bias \pm standard deviation.

339

340

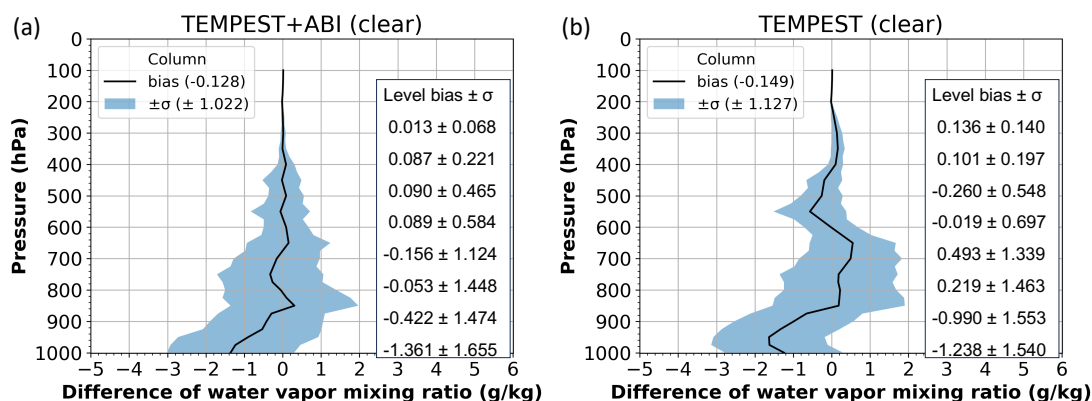
341 4.1.2. Statistics

342

343 Comparisons of humidity retrievals using merged five TEMPEST MW bands and three ABI-sounding
 344 channels (6.2, 6.9, and 7.3 μm) versus using only the TEMPEST sensor are performed for 1000
 345 randomly selected clear sky cases. Results are shown in Fig. 6. As with the case studies, adding three
 346 ABI channels clearly reduces layer biases and random errors in the retrieved water vapor profiles.
 347 Errors in the retrieved water vapor above 800 hPa are significantly smaller when using the five MW
 348 bands from TEMPEST in combination with the three ABI channels. While the overall water vapor biases
 349 and standard deviations under clear conditions are reduced only slightly from $(-0.149 \pm 1.127 \text{ g/kg})$ for



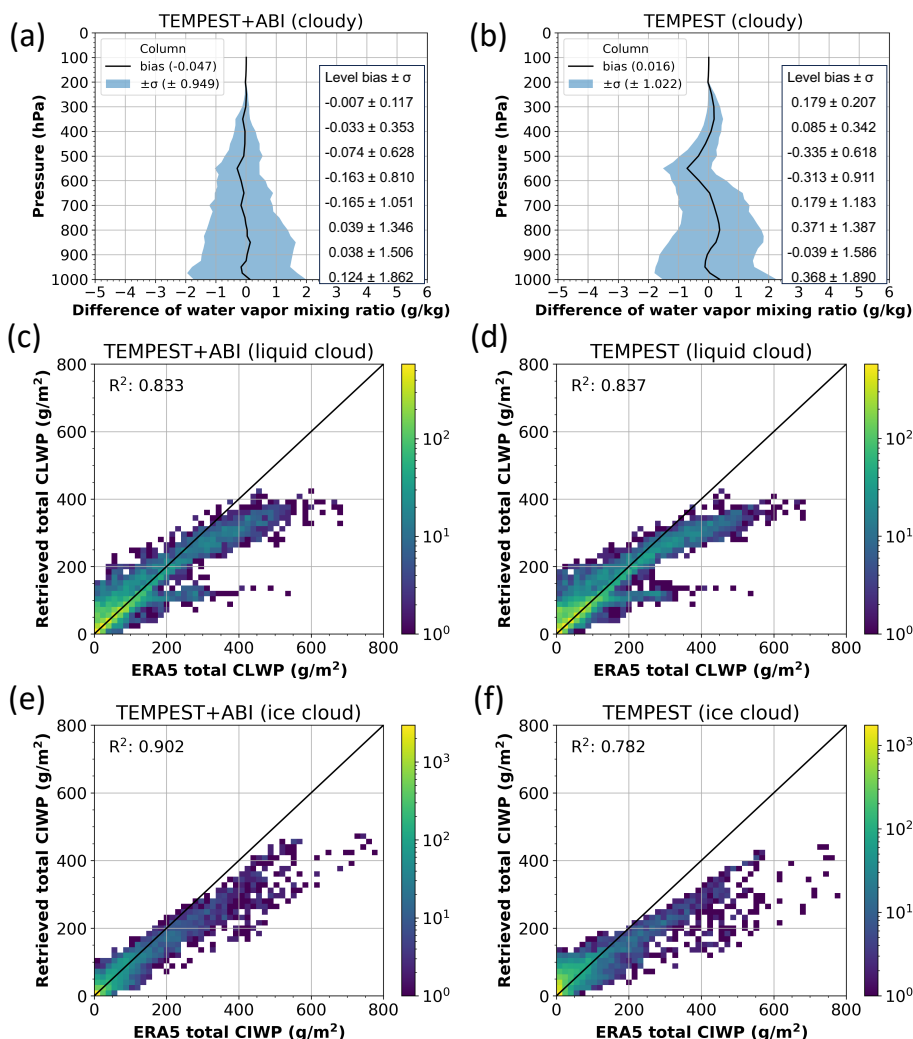
350 TEMPEST only to $(-0.128 \pm 1.022 \text{ g/kg})$ for TEMPEST+ABI, much larger reductions can be seen in the
 351 layer values shown in Fig. 6 – starting at 900 hPa and extending all the way to 300 hPa.
 352
 353



354 Figure 6. Sensitivity tests of retrieving water vapor profiles using the synthetic measurement from
 355 ERA5 under clear conditions over the ocean on 2020/05/27. Figure (a) shows retrievals using TEMPEST
 356 and ABI combined channels, and retrievals using only TEMPEST channels are for Figure (b). Figures (a)
 357 and (b) show the difference in water vapor mixing ratio from 1000 randomly selected profiles between
 358 retrievals and ERA5 (retrievals minus ERA5) along the height. The solid black lines are the bias value,
 359 and the blue shade area is the standard deviation (σ). The included table quantifies the retrieval
 360 performance from 300 to 1000 hPa for every 100 hPa.
 361

362
 363
 364 Similarly, the accuracy of humidity retrievals from 1000 randomly selected cloudy cases using two
 365 different sensor configurations is shown in Figs. 7(a) and 7(b). Consistent with the case study and clear
 366 sky cases shown in Fig. 6, adding three ABI IR channels to the retrievals also reduces biases in the mid-
 367 tropospheric layers for cloudy scenes. Due to the lack of sensitivity of three ABI-sounding channels to
 368 the lower atmosphere in the cloudy case, as shown in Fig. 3(c), the performance of water vapor
 369 retrievals around the surface shows only a negligible improvement. While the column metrics show
 370 unbiased results with or without ABI, the standard deviation of retrieval errors is larger when using
 371 TEMPEST-only retrievals (1.022 g/kg) than using merged TEMPEST and ABI channels (0.949 g/kg).
 372 Quantitative comparisons of the vertical profiles in Figs. 7(a) and 7(b) again reveal that the layer
 373 biases are significantly reduced in the TEMPEST+ABI retrievals relative to TEMPEST alone, reducing the
 374 individual layer biases by approximately 50 % (although not uniformly in all layers). The overall biases
 375 are smaller than in the clear case. The latter is explained by the fact that the a priori guess comes from
 376 the climatology of ERA5 profiles for the month, and these profiles overwhelmingly contain clouds. The
 377 cloudy retrieval is thus less biased in the initial iteration, while the clear retrievals must adjust the first
 378 guess to correspond to drier conditions when the atmosphere is cloud-free. Standard deviations are
 379 slightly larger for cloudy scenes, as should be expected from a more complex retrieval.

380
 381



382
 383 Figure 7. Sensitivity tests of retrievals of water vapor, liquid and ice clouds using synthetic observations
 384 from ERA5 under cloudy conditions over the ocean on 2020/05/27. Figures (a), (c), and (e) show
 385 retrievals using TEMPEST and ABI combined channels, and retrievals using only TEMPEST channels are
 386 for Figures (b), (d), and (f). Figures (a) and (b) show the difference in water vapor mixing ratio from
 387 1000 randomly selected profiles between retrievals and ERA5 (retrievals minus ERA5) along the height.
 388 The solid black lines are the bias value, and the blue shade area is the standard deviation (σ). The
 389 included table quantifies the retrieval performance from 300 to 1000 hPa for every 100 hPa. Figures (c)
 390 and (d) are two-dimensional histograms of retrieved and ERA5 total cloud liquid water path from 8000
 391 randomly selected cases. R^2 is the coefficient of determination. Color means the number of samples;
 392 the solid black lines are the one-to-one lines. Figures (e) and (f) are the same as Figures (c) and (d) but
 393 for the total cloud ice water path.

394
 395

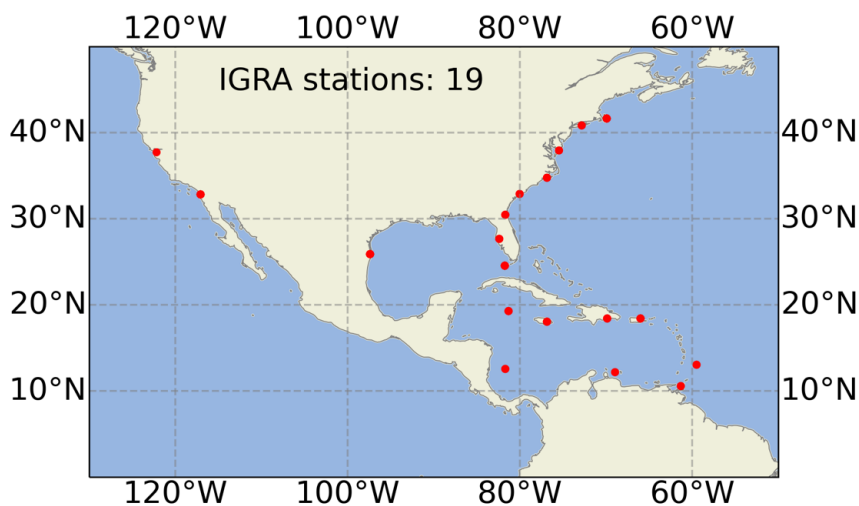


396 The performance of liquid and ice cloud retrievals is shown in Figs. 7(c) to 7(f). Compared with the
397 cloud liquid water path from ERA5, the liquid cloud retrievals do not improve after incorporating three
398 more ABI-sounding channels shown in Figs. 7(c) and 7(d), as the cloud liquid water path signal is
399 confined almost entirely to the 87 and 164 GHz channels of TEMPEST-D. The sensitivity to liquid clouds
400 with and without ABI channels is similar, with R^2 values about 0.83. Since ice clouds are at a higher
401 altitude and interact with the water-vapor-sounding channels, the 164 to 181 GHz TEMPEST and 6.2 to
402 7.3 μm ABI channels have different degrees of sensitivity, as shown in Fig. 3(c). Adding three ABI-
403 sounding channels has larger impacts on the retrieved ice clouds, as the R^2 values increase from 0.782
404 using only TEMPEST bands to about 0.9 using eight combined channels from TEMPEST and ABI. Despite
405 the ability to detect ice clouds, the IR-sounding channels have little information about the ice water
406 content that is available from the MW alone. Overall, the retrieved liquid and ice clouds are all
407 underestimated compared with the ERA5 profiles. For liquid clouds, this is simply due to the saturation
408 of the cloud water emission signal at roughly 300 to 400 g/m^2 with the available channels. For ice
409 clouds, the primary signal is a brightness temperature depression due to scattering. While this signal
410 does not saturate, thicker ice clouds (> 300 to 400 g/m^2) are often found in conjunction with liquid
411 clouds in ERA5, leading to brightness temperature signatures that are more difficult to untangle.

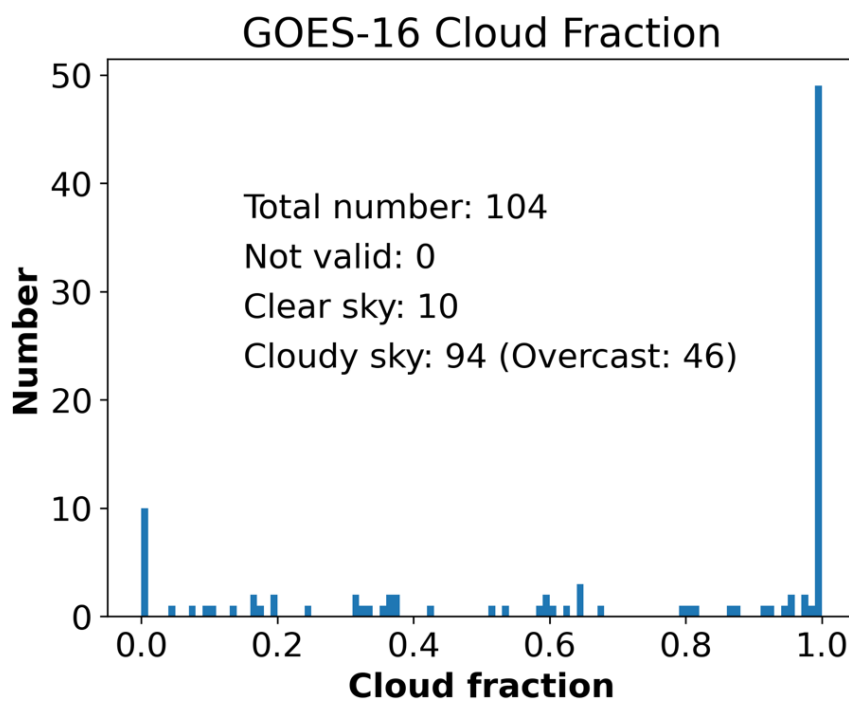
412 413 **4.2. Independent Validation**

414
415 While the preceding section focused on synthetic brightness temperatures generated from ERA5
416 profiles, this section uses radiosonde data to validate retrievals from actual observations. The
417 Integrated Global Radiosonde Archive (IGRA) has collected and quality-controlled in situ observations
418 from over 2,800 global stations since 1905, providing vertical profiles of pressure, temperature,
419 humidity, and wind speed and direction. The IGRA dataset can be accessed at
420 <https://www.ncei.noaa.gov/products/weather-balloon/integrated-global-radiosonde-archive>. The
421 IGRA dataset used in the study is version 2.2 and is collocated with TEMPEST-D and GOES-16 ABI
422 observations from 2019 to 2020. To ensure consistency in collocated cases, the observations from
423 these three datasets are all within 1 hour and 1 degree latitude/longitude. Because the OE retrieval
424 discussed here is limited to oceans, the radiosondes used in this study are limited to coastal regions. To
425 avoid surface contaminations, the collocated TEMPEST-D measurements are moved over the ocean to
426 ensure that ~ 30 km (the sensor field of view) in all directions of the TEMPEST-D pixel is free of land.
427 The displaced footprints must have the same cloud conditions (clear sky or cloudy) as determined by
428 GOES-16 cloud products at the radiosonde location to ensure these locations are under similar
429 atmospheric conditions. There are 19 collocated coastal IGRA stations in the GOES-16 field of view, as
430 shown in Fig. 8. The collocated IGRA sites are around North America and the Caribbean Sea. Given
431 GOES-16 cloud information, there are 104 collocated cases, of which 10 cases are cloud-free, and 94
432 cases are under different degrees of cloudy skies, as shown in Fig. 9. The limited number of coincident
433 samples is due to infrequent TEMPEST-D overpasses coupled with infrequent (twice daily) radiosonde
434 launches and frequent data downlink problems of TEMPEST-D, leaving only this limited set of
435 radiosondes to compare to.

436
437



438
439 Figure 8. Map of collocated IGRA stations. The total number of collocated sites is 19, as marked in the
440 red circle dots.
441
442



443
444 Figure 9. The histogram of GOES-16 derived cloud fraction at the collocated locations. The total
445 number of collocated cases is 104, including 10 clear and 94 cloudy cases.
446



447

448 With additional cloud information from GOES-16 products, water vapor retrievals are validated with
449 various levels of cloud information from the geostationary observations, as described in Table 1. The
450 most significant difference is that the algorithm does not retrieve clouds when the area is cloud-free
451 (as determined by ABI's cloud mask) and uses observations from all channels to retrieve water vapor
452 profiles only. Figure 10 shows the error in the retrieved water vapor profiles in clear skies, with biases
453 and standard deviations of column errors listed in Table 2. Only nine cases converged among ten clear
454 sky cases under four different retrieval settings. The convergence criteria from Eq. (2) are set to 0.8 for
455 retrievals using TEMPEST-D and ABI eight channels and are 0.5 for using TEMPEST-D five bands, as
456 mentioned in section 3 (either 5 or 8 layers of clouds/water vapor in this case).

457

458

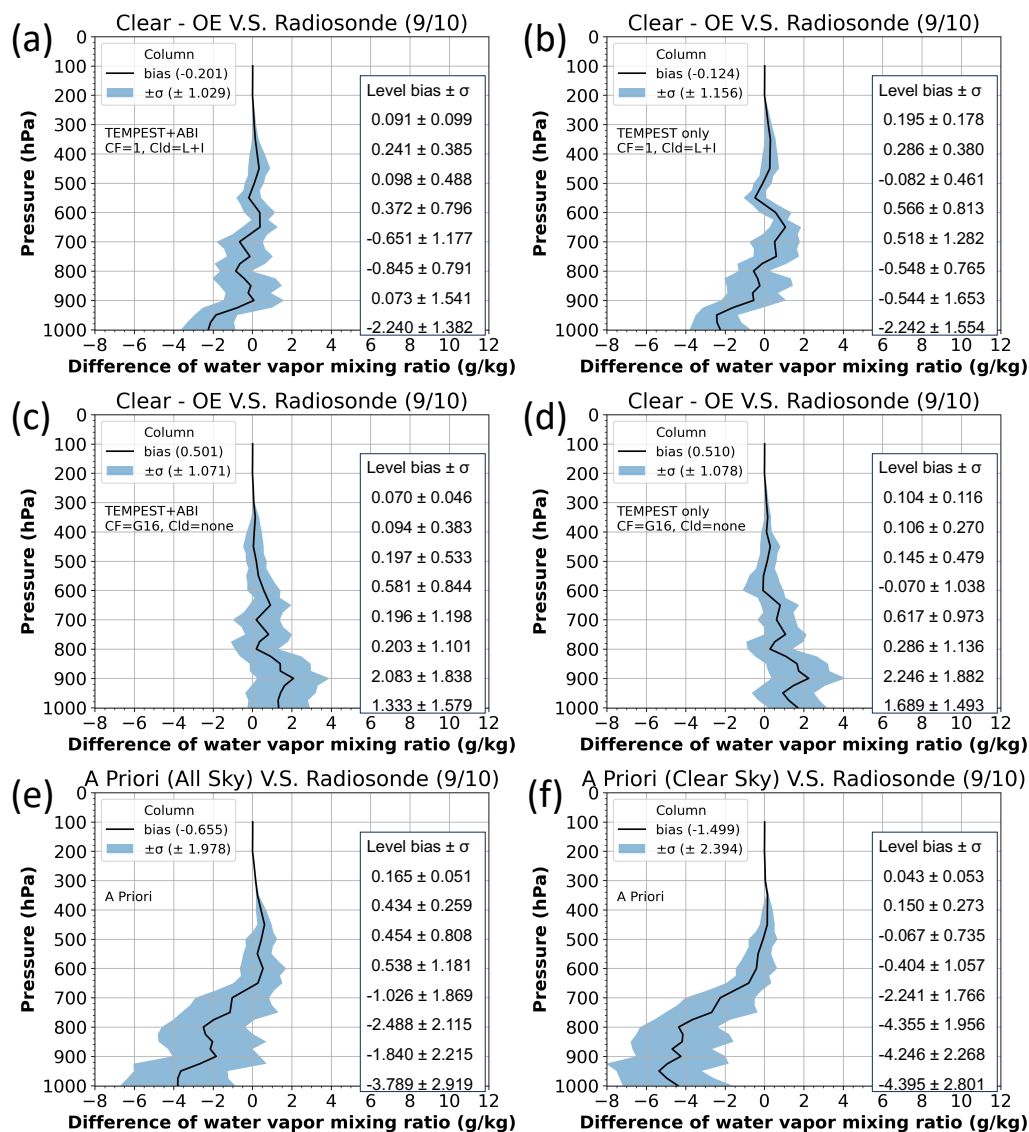
459 Table 2. Compared with IGRA radiosonde observations, the column bias and standard deviation of
460 retrieved water vapor mixing ratio under the clear sky conditions. The statistic values are evaluated
461 based on all converged nine clear sky cases. CF means cloud fraction.

462

Sensors	Using GOES-16 cloud products	
	No set CF to 1	Yes set CF to 0
TEMPEST+ABI (8 channels)	-0.201 ± 1.029 g/kg	0.501 ± 1.071 g/kg
TEMPEST (5 channels)	-0.124 ± 1.156 g/kg	0.510 ± 1.078 g/kg

463

464

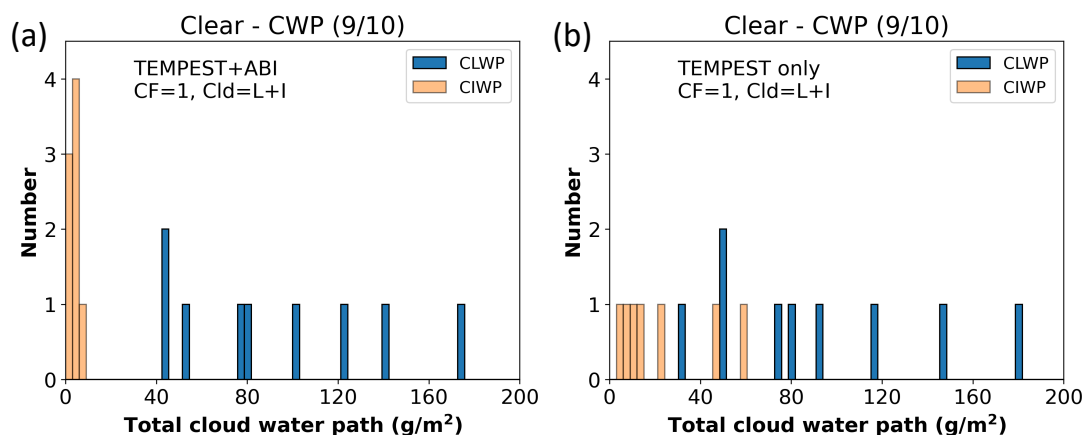


465
 466 Figure 10. The water vapor mixing ratio difference between retrievals and radiosonde measurement
 467 (retrievals minus IGRA) in the GOES-16 observed clear skies. Retrievals use bands from TEMPEST-D and
 468 GOES-16 ABI in Figures (a) and (c) and use only TEMPEST-D channels in Figures (b) and (d). Retrievals in
 469 Figures (a) and (b) assume existing liquid and ice clouds with cloud fraction = 1, and retrievals in Figures
 470 (c) and (d) set no clouds with cloud fraction = 0. In the retrievals, the biases of the water vapor a priori
 471 information derived from all-sky conditions are shown in Figure (e), and obtained from clear skies are
 472 presented in Figure (f). The solid black lines are the bias value, and the blue shade regions indicate the
 473 standard deviation (σ). The included table quantifies the retrieval performance from 300 to 1000 hPa
 474 for every 100 hPa. The number in the parentheses indicates the number of all converged cases out of
 475 all clear sky cases. G16 means GOES-16 products, and L+I indicates liquid and ice clouds.



476
 477
 478
 479
 480
 481
 482
 483
 484
 485
 486
 487
 488
 489
 490
 491
 492
 493
 494
 495
 496

The three additional water-vapor-sounding channels from ABI help to constrain water vapor profiles, as shown in the reduced column error standard deviations as well as the layer biases and standard deviations, although the differences are smaller than they were with the simulated results. Compared with TEMPEST-only (Figs. 10(b) and 10(d)), the retrieved water vapor profiles above 800 hPa are visibly less biased after including ABI channels (Figs. 10(a) and 10(c)). The overall statistics are not as impressive because much of the water vapor is in the 1000 to 800 hPa layer that is not improved by additional ABI channels. Figures 11(a) and 11(b) present the erroneous retrieved liquid and ice clouds under the clear conditions corresponding to Figs. 10(a) and 10(b), respectively. No clouds are estimated in retrievals in Figs. 10(c) and 10(d), as this information is taken from the IR channels. Because parts of the water vapor signals are falsely attributed to clouds, retrieved water vapor profiles are underestimated when clouds are derived, as in Figs. 10(a), 10(b), and 11. On the other hand, retrieved water vapor profiles are overestimated in Figs. 10(c) and 10(d) when the scene is forced to be cloud-free based on ABI information. We speculate that, as with the synthetic retrievals, the bias from ERA5 information in Fig. 10(f) under clear sky assumptions is even larger than if all sky ERA5 a priori in Fig. 10(e) is used. This leads to even larger biases in the initial iteration, which the retrievals can only partially correct without adding small amounts of cloud water to the scene. Conversely, it is also possible that the small number of cases (9) simply are not representative.



497
 498
 499
 500
 501
 502
 503
 504
 505
 506

Figure 11. Retrieved total cloud water path for liquid and ice clouds in the clear sky cases with no cloud information from GOES-16. Retrievals in Figure (a) use channels from TEMPEST-D and ABI and use only TEMPEST-D channels for Figure (b). The number in the parentheses indicates the number of all converged cases among all clear sky cases. L+I indicates liquid and ice clouds.

Water vapor retrieval errors under cloudy conditions for various assumptions of cloud knowledge are presented in Fig. 12, with the corresponding bias and standard deviation of column errors listed in Table 3. The retrieval configurations in cloudy cases are listed in Table 1. Retrievals in Figs. 12(a) and



507 12(b) have no information about clouds. In contrast, Figs. 12(c) to 12(f) show results with different
 508 degrees of knowledge about clouds from ABI. Figures 12(c) and 12(d) use only cloud fractions. While
 509 column average water vapor retrievals do not improve significantly by adding cloud fraction
 510 information, quantitative comparisons included in Figs. 12(a) through 12(d) paint a consistent picture
 511 of improvement above 800 hPa for both TEMPEST-only and TEMPEST+ABI when cloud fractions are
 512 specified. The water vapor retrieval errors are further decomposed by cloud fraction from GOES-16,
 513 shown in Fig. 13, using various retrieval configurations shown in Table 1 under cloudy conditions.
 514 Among six retrieval settings, the estimated water vapor profiles are nearly unbiased when the cloud
 515 fraction is between 0.4 and 0.6 with about 0.5 g/kg of error standard deviation, as these amounts of
 516 clouds provide enough signals and do not entirely obscure signals underneath. For low cloud fractions,
 517 assigning the correct cloud fraction from GOES-16 ABI leads to a bias, although the standard deviation
 518 is roughly the same as if a cloud fraction of 1 is assigned. This can be attributed to the nonlinear
 519 response of the MW radiances at 87 and 164 GHz to cloud water content. When the assigned cloud
 520 fraction is too small, the retrieval must assign all the necessary cloud liquid water to a small cloud
 521 fraction, saturating the radiance signals and generally causing poorer retrievals. As was seen in the
 522 synthetic retrievals, saturation will cause the cloud water to be underestimated, which will in turn lead
 523 to an overestimation in water vapor as the OE tries to balance all radiance terms. If the scene is truly
 524 overcast (observed cloud fraction near 1.0), there can be no difference between assigning a cloud
 525 fraction of 1.0 as the default assumption or 1.0 as an observed parameter, and this is reflected in the
 526 results as well.

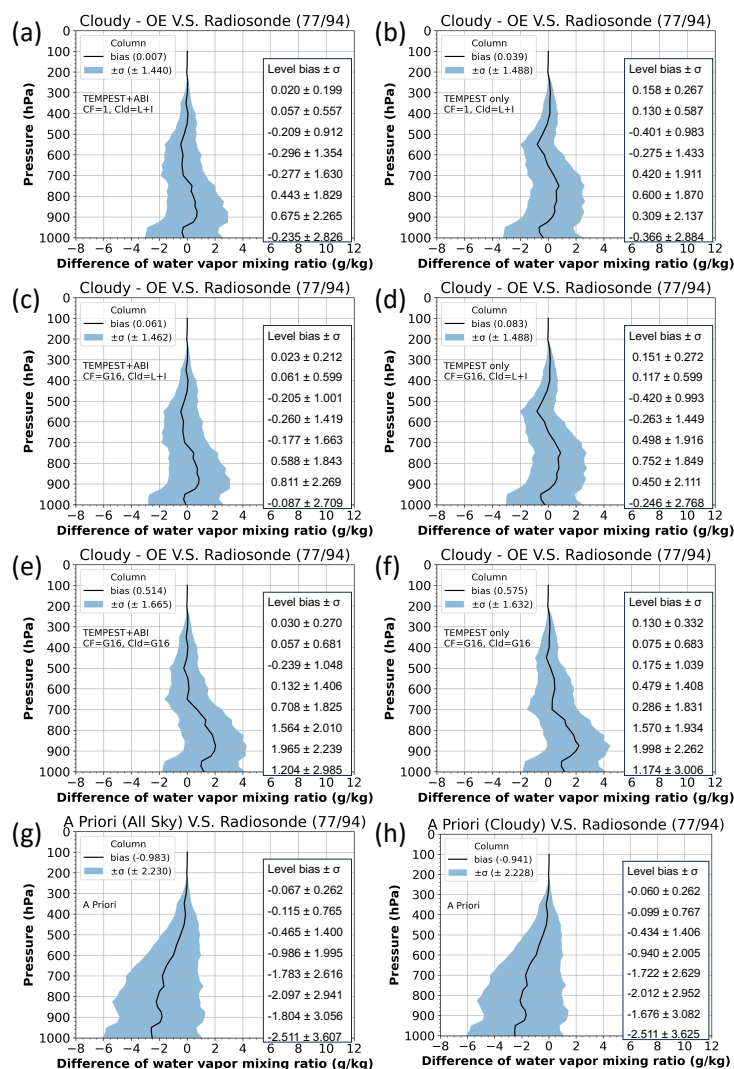
527
 528 Additional cloud information in the form of cloud fraction, cloud height, and cloud phase from GOES-16
 529 products are shown in Figs. 12(e) and 12(f). When retrievals use more cloud information from GOES-16
 530 (cloud fraction, height, and phase), column water vapor retrievals shown in Figs. 12(e) and 12(f) are
 531 less biased above 700 hPa when compared to Figs. 12(a) to 12(d), but lower layers show larger biases
 532 and little difference between using only TEMPEST or TEMPEST+ABI. In cloudy conditions, the only
 533 channels with sensitivity to the low-level water vapor are the TEMPEST 87 and 164 GHz channels, as
 534 shown in Fig. 3(c). However, some overfitting appears to be taking place. The authors speculate that
 535 the ice scattering properties assumed in the retrieval's forward model may cause excess depression at
 536 87 and 164GHz channels, which in turn, requires the algorithm to increase the cloud water and water
 537 vapor to match the brightness temperatures in those channels.

538
 539 Table 3. Column bias and standard deviation of retrieved water vapor mixing ratio in the cloudy skies
 540 when compared to IGRA radiosonde observations. Statistics are evaluated based on all converged 77
 541 cloudy sky cases.

542

Sensors	Using GOES-16 cloud products		
	No set CF to 1	Yes set CF from GOES-16	Yes set CF, CH, and CP from GOES-16
TEMPEST+ABI (8 channels)	0.007 ± 1.440 g/kg	0.061 ± 1.462 g/kg	0.514 ± 1.665 g/kg
TEMPEST (5 channels)	0.039 ± 1.488 g/kg	0.083 ± 1.488 g/kg	0.575 ± 1.632 g/kg

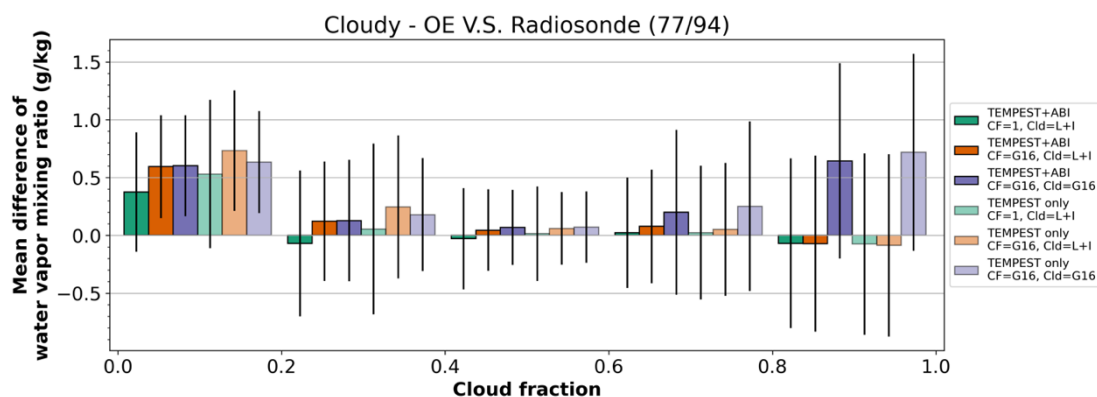
543



544
 545 Figure 12. The water vapor mixing ratio difference between retrievals and radiosonde measurement
 546 (retrievals minus IGRA) with GOES-16 observed cloudy conditions. Retrievals use bands from TEMPEST-
 547 D and GOES-16 ABI in Figures (a), (c), and (e) and use only TEMPEST-D channels in Figures (b), (d), and
 548 (f). Figures (a) to (d) show retrievals assuming liquid and ice clouds with cloud fraction = 1 for Figures
 549 (a) and (b) and with cloud fraction from GOES-16 cloud mask for Figures (c) and (d). Retrievals in
 550 Figures (e) and (f) use cloud fraction, height, and phase from GOES-16 products to define cloud layers.
 551 In the retrievals, the biases of the water vapor a priori information derived from all-sky conditions are
 552 shown in Figure (g), and obtained from all sky v.s. radiosonde are presented in Figure (h). The solid black lines
 553 are the bias value, and the blue shade regions indicate the standard deviation (σ). The included table
 554 quantifies the retrieval performance from 300 to 1000 hPa for every 100 hPa. The number in the
 555 parentheses means the number of all converged cases out of all cloudy sky cases. G16 means GOES-16
 556 products, and L+I indicates liquid and ice clouds.



557
558



559
560
561
562
563
564
565
566
567
568
569
570

Figure 13. The mean difference between retrieved and radiosonde-observed water vapor profiles (retrievals minus IGRA) within different GOES-16 cloud fraction intervals. Assuming both liquid and ice clouds exist, the green bars indicate that retrievals use cloud fraction = 1, and the orange bars mean that retrievals use only cloud fraction from GOES-16 products. The purple bars show retrievals using cloud fraction, height, and phase from GOES-16 products. Lighter colors mean retrievals only use TEMPEST-D, and darker colors show retrievals using both TEMPEST-D and GOES-16 ABI sensors. Solid black lines are the range of \pm standard deviation. The number in the parentheses means the number of all converged cases among all cloudy sky cases. G16 means GOES-16 products, and L+I indicates liquid and ice clouds.

5. Conclusions

571
572
573
574
575
576
577
578
579
580
581
582

TEMPEST-D successfully demonstrated the capability of CubeSats radiometers to maintain well-calibrated MW signals in five channels from 87 to 181 GHz over a period of almost 3 years. Although TEMPEST-D and the TEMPEST instrument currently flying with COWVR on the International Space Station are economical and functional, these small MW radiometers fly without an accompanying hyperspectral IR sensor typical on operational platforms. GOES-R ABI sensors provide observations of the Earth every 1 to 10 minutes depending on the modes, and measure 16 spectral bands from VIS to IR with 0.5 to 2.0 km ground resolution. Given such unique ABI observations with high spatial and temporal resolution, supplemental information from ABI enhances the ability of TEMPEST as well as other similar CubeSats to infer the states of the atmosphere.

583
584
585
586
587
588
589

Along with five TEMPEST MW bands, this study presented improvements in humidity profiles that are possible when TEMPEST retrievals are supplemented with three IR water-vapor-sounding channels available from GOES ABI. A number of positive outcomes were shown in this paper. In the sensitivity tests comparing the combined MW/IR retrievals to MW-only capabilities, the effective vertical resolution increases, as seen by smaller layer errors, under both clear and cloudy conditions. The retrieved water vapor profiles were validated using independent IGRA humidity-sounding data from 2019 to 2020. During these two years of routine TEMPEST-D operations, only 104 IGRA cases (10 cases



590 are clear scenes, 94 under different cloudy conditions) exist. Consistent with the sensitivity tests, the
591 validation also showed the advantages of using GOES-16 cloud products and three additional ABI IR
592 channels in water vapor sounding under different sky conditions.

593

594 In clear sky regions, with ABI's ability to unambiguously characterize these scenes as cloud-free,
595 retrievals are improved merely by forcing the scene to be cloud-free. While statistics in Figs. 10 and 11
596 indicate that column average biases grow slightly when ABI is used to identify the scene as cloud-free,
597 the profiles themselves show clear improvement above the boundary layer. Near the surface,
598 retrievals are sensitive to the large biases in the prior data in these comparisons, and it is difficult to
599 draw conclusions. Nonetheless, adding three ABI channels slightly decreased overall biases from 0.510
600 to 0.501 g/kg with about the same error standard deviation of 1 g/kg.

601

602 Under cloudy conditions, water vapor retrievals are significantly improved when adding ABI, as shown
603 in Figs. 12 and 13, and results are generally improved when cloud fraction information is added to the
604 retrieval, except for very small cloud fractions where saturation in the cloudy portion of the footprint
605 becomes an issue. Adding cloud top and cloud phase information causes errors larger than 0.5 g/kg.
606 This is likely due to incorrect assumptions about the ice cloud scattering properties.

607

608 This study explored the advantages of merging TEMPEST-D, with ABI observations from GOES-16 to
609 improve water vapor soundings. However, ABI-like sensors, whether on the Himawari series satellites
610 (Bessho et al., 2016), or other platforms, cover the entire globe, providing multi-spectral, high spatial,
611 and high temporal observations. With more and more CubeSats being launched, including COWVR and
612 TEMPEST on Space Test Program-Houston 8 (<https://podaac.jpl.nasa.gov/COWVR-TEMPEST>), TROPICS
613 (Blackwell et al., 2018; <https://tropics.ll.mit.edu/CMS/tropics>), and the INvestigation of Convective
614 Updrafts (INCUS; van den Heever et al., 2022; <https://incus.colostate.edu>) missions, these missions will
615 all benefit from more sounding and cloud information from ABI-like sensors, enhancing the capability
616 of CubeSats.

617

618 **Code availability**

619

620 CRTM is available through the website <https://github.com/JCSDA/crtm>, and MonoRTM can be assessed
621 by the website http://rtweb.aer.com/monortm_frame.html.

622

623 **Data availability**

624

625 The TEMPEST-D datasets can be downloaded through the website <https://tempest.colostate.edu> after
626 registration. The GOES-16 products are archived at CLASS (<https://www.avl.class.noaa.gov>). The IGRA
627 dataset is available at [https://www.ncei.noaa.gov/products/weather-balloon/integrated-global-](https://www.ncei.noaa.gov/products/weather-balloon/integrated-global-radiosonde-archive)
628 [radiosonde-archive](https://www.ncei.noaa.gov/products/weather-balloon/integrated-global-radiosonde-archive). The ERA5 dataset can be accessed by the website
629 <https://www.ecmwf.int/en/forecasts/dataset/ecmwf-reanalysis-v5>.

630

631 **Author contribution**

632



633 CPK and CK designed and improved the experiments. CPK is responsible for collecting and processing
634 data. CPK prepared the manuscript. CPK and CK discussed the results and revised the manuscript.

635

636 **Competing interests**

637

638 The contact author has declared that none of the authors has any competing interests.

639

640 **Acknowledgments**

641

642 This study was supported by NASA grant 80NM0078F0617 as part of an effort to improve water vapor
643 soundings from the TEMPEST CubeSat radiometer on Space Test Program-Houston 8.

644



645 **References**

646

647 Aires, F.: Measure and exploitation of multisensor and multiwavelength synergy for remote sensing: 1.
648 Theoretical considerations, *J. Geophys. Res.*, 116, D02301–D02301,
649 <https://doi.org/10.1029/2010JD014701>, 2011.

650

651 Aires, F., Paul, M., Prigent, C., Rommen, B., and Bouvet, M.: Measure and exploitation of multisensor
652 and multiwavelength synergy for remote sensing: 2. Application to the retrieval of atmospheric
653 temperature and water vapor from MetOp, *J. Geophys. Res.*, 116, D02302–D02302,
654 <https://doi.org/10.1029/2010JD014702>, 2011.

655

656 Aires, F., Aznay, O., Prigent, C., Paul, M., and Bernardo, F.: Synergistic multi-wavelength remote sensing
657 versus a posteriori combination of retrieved products: Application for the retrieval of atmospheric
658 profiles using MetOp-A, *J. Geophys. Res.*, 117, D18304, <https://doi.org/10.1029/2011JD017188>, 2012.

659

660 Berg, W., Brown, S. T., Lim, B. H., Reising, S. C., Goncharenko, Y., Kummerow, C. D., Gaier, T. C., and
661 Padmanabhan, S.: Calibration and validation of the TEMPEST-D CubeSat radiometer, *IEEE Trans.*
662 *Geosci. Remote Sens.*, 59, 4904–4914, <https://doi.org/10.1109/TGRS.2020.3018999>, 2021.

663

664 Bessho, K., Date, K., Hayashi, M., Ikeda, A., Imai, T., Inoue, H., Kumagai, Y., Miyakawa, T., Murata, H.,
665 Ohno, T., Okuyama, A., Oyama, R., Sasaki, Y., Shimazu, Y., Shimoji, K., Sumida, Y., Suzuki, M., Taniguchi,
666 H., Tsuchiyama, H., Uesawa, D., Yokota, H., and Yoshida, R.: An introduction to Himawari-8/9 - Japan's
667 new-generation geostationary meteorological satellites, *J. Meteorolog. Soc. Jpn.*, 94, 151–183,
668 <https://doi.org/10.2151/jmsj.2016-009>, 2016.

669

670 Blackwell, W. J., Braun, S., Bennartz, R., Velden, C., DeMaria, M., Atlas, R., Dunion, J., Marks, F., Rogers,
671 R., Annane, B., and Leslie, R. V.: An overview of the TROPICS NASA Earth Venture Mission, *Q. J. R.*
672 *Meteorolog. Soc.*, 144, 16–26, <https://doi.org/10.1002/qj.3290>, 2018.

673

674 Bohren, C. F. and Huffman, D. R.: *Absorption and Scattering of Light by Small Particles*, Wiley, New
675 York, 530 pp., <https://doi.org/10.1002/9783527618156>, 1998.

676

677 Boukabara, S.-A., Garrett, K., Chen, W., Iturbide-Sanchez, F., Grassotti, C., Kongoli, C., Chen, R., Liu, Q.,
678 Yan, B., Weng, F., Ferraro, R., Kleespies, T. J., and Meng, H.: MiRS: An all-weather 1DVAR satellite data
679 assimilation and retrieval system, *IEEE Trans. Geosci. Remote Sens.*, 49, 3249–3272,
680 <https://doi.org/10.1109/TGRS.2011.2158438>, 2011.

681

682 Boukabara, S.-A., Garrett, K., Grassotti, C., Iturbide-Sanchez, F., Chen, W., Jiang, Z., Clough, S. A., Zhan,
683 X., Liang, P., Liu, Q., Islam, T., Zubko, V., and Mims, A.: A physical approach for a simultaneous retrieval
684 of sounding, surface, hydrometeor, and cryospheric parameters from SNPP/ATMS, *J. Geophys. Res.:*
685 *Atmos.*, 118, 12,600–12,619, <https://doi.org/10.1002/2013JD020448>, 2013.

686



- 687 Boukabara, S.-A., Garrett, K., and Grassotti, C.: Dynamic inversion of global surface microwave
688 emissivity using a 1DVAR approach, *Remote Sens.*, 10, 679–679, <https://doi.org/10.3390/rs10050679>,
689 2018.
690
- 691 Brown, S. T., Tanner, A., Reising, S. C., and Berg, W.: Single-point calibration for microwave sounders:
692 Application to TEMPEST-D, *J. Atmos. Oceanic Technol.*, <https://doi.org/10.1175/JTECH-D-22-0063.1>,
693 2023.
694
- 695 Clough, S. A., Shephard, M. W., Mlawer, E. J., Delamere, J. S., Iacono, M. J., Cady-Pereira, K.,
696 Boukabara, S., and Brown, P. D.: Atmospheric radiative transfer modeling: A summary of the AER
697 codes, *J. Quant. Spectrosc. Radiat. Transfer*, 91, 233–244, <https://doi.org/10.1016/j.jqsrt.2004.05.058>,
698 2005.
699
- 700 Draine, B. T. and Flatau, P. J.: Discrete-dipole approximation for scattering calculations, *J. Opt. Soc. Am.*
701 *A*, 11, 1491, <https://doi.org/10.1364/JOSAA.11.001491>, 1994.
702
- 703 Duncan, D. I. and Kummerow, C. D.: A 1DVAR retrieval applied to GMI: Algorithm description,
704 validation, and sensitivities, *J. Geophys. Res.: Atmos.*, 121, 7415–7429,
705 <https://doi.org/10.1002/2016JD024808>, 2016.
706
- 707 Elsaesser, G. S. and Kummerow, C. D.: Toward a fully parametric retrieval of the nonraining parameters
708 over the global oceans, *J. Appl. Meteorol. Climatol.*, 47, 1599–1618,
709 <https://doi.org/10.1175/2007JAMC1712.1>, 2008.
710
- 711 Field, P. R., Heymsfield, A. J., and Bansemer, A.: Snow size distribution parameterization for midlatitude
712 and tropical ice clouds, *J. Atmos. Sci.*, 64, 4346–4365, <https://doi.org/10.1175/2007JAS2344.1>, 2007.
713
- 714 Gambacorta, A., Barnet, C., Wolf, W., Goldberg, M., King, T., Ziong, X., Nalli, N., Maddy, E., and
715 Divakarla, M.: The NOAA Unique CrIS/ATMS Processing System (NUCAPS): First light retrieval results,
716 in: In Proceedings of the ITWG meeting, ITWG, Toulouse, France, 2012.
717
- 718 Goodman, S. J., Schmit, T. J., Daniels, J., and Redmon, R. J. (Eds.): *The GOES-R Series: A New Generation*
719 *of Geostationary Environmental Satellites*, Elsevier, <https://doi.org/10.1016/C2015-0-06249-9>, 2019.
720
- 721 Hersbach, H., Bell, B., Berrisford, P., Hirahara, S., Horányi, A., Muñoz-Sabater, J., Nicolas, J., Peubey, C.,
722 Radu, R., Schepers, D., Simmons, A., Soci, C., Abdalla, S., Abellan, X., Balsamo, G., Bechtold, P., Biavati,
723 G., Bidlot, J., Bonavita, M., Chiara, G., Dahlgren, P., Dee, D., Diamantakis, M., Dragani, R., Flemming, J.,
724 Forbes, R., Fuentes, M., Geer, A., Haimberger, L., Healy, S., Hogan, R. J., Hólm, E., Janisková, M., Keeley,
725 S., Laloyaux, P., Lopez, P., Lupu, C., Radnoti, G., Rosnay, P., Rozum, I., Vamborg, F., Villaume, S., and
726 Thépaut, J.: The ERA5 global reanalysis, *Q. J. R. Meteorolog. Soc.*, 146, 1999–2049,
727 <https://doi.org/10.1002/qj.3803>, 2020.
728



- 729 Johnson, B. T., Dang, C., Stegmann, P., Liu, Q., Moradi, I., and Auligne, T.: The Community Radiative
730 Transfer Model (CRTM): Community-focused collaborative model development accelerating research
731 to operations, *Bull. Am. Meteorol. Soc.*, <https://doi.org/10.1175/BAMS-D-22-0015.1>, 2023.
732
- 733 Kazumori, M. and English, S. J.: Use of the ocean surface wind direction signal in microwave radiance
734 assimilation, *Q. J. R. Meteorolog. Soc.*, 141, 1354–1375, <https://doi.org/10.1002/qj.2445>, 2015.
735
- 736 Kulie, M. S., Bennartz, R., Greenwald, T. J., Chen, Y., and Weng, F.: Uncertainties in microwave
737 properties of frozen precipitation: Implications for remote sensing and data assimilation, *J. Atmos. Sci.*,
738 67, 3471–3487, <https://doi.org/10.1175/2010JAS3520.1>, 2010.
739
- 740 Li, J., Schmit, T. J., Jin, X., Martin, G., and Li, Z.: GOES-R Advanced Baseline Imager (ABI) Algorithm
741 Theoretical Basis Document for Legacy Atmospheric Moisture Profile, Legacy Atmospheric
742 Temperature Profile, Total Precipitable Water, and Derived Atmospheric Stability Indices, Version 3.1,
743 2019.
744
- 745 Liu, G.: A database of microwave single-scattering properties for nonspherical ice particles, *Bull. Am.*
746 *Meteorol. Soc.*, 89, 1563–1570, <https://doi.org/10.1175/2008BAMS2486.1>, 2008.
747
- 748 Liu, Q., van Delst, P., Chen, Y., Groff, D., Han, Y., Collard, A., Weng, F., Boukabara, S.-A., and Derber, J.:
749 Community Radiative Transfer Model for radiance assimilation and applications, in: IGARSS 2012 - 2012
750 IEEE International Geoscience and Remote Sensing Symposium, Munich, Germany, 3700–3703,
751 <https://doi.org/10.1109/IGARSS.2012.6350612>, 2012.
752
- 753 Ma, Z., Li, Z., Li, J., Schmit, T. J., Cucurull, L., Atlas, R., and Sun, B.: Enhance low level temperature and
754 moisture profiles through combining NUCAPS, ABI observations, and RTMA analysis, *Earth Space Sci.*, 8,
755 <https://doi.org/10.1029/2020EA001402>, 2021.
756
- 757 Milstein, A. B. and Blackwell, W. J.: Neural network temperature and moisture retrieval algorithm
758 validation for AIRS/AMSU and CrIS/ATMS, *J. Geophys. Res.: Atmos.*, 121, 1414–1430,
759 <https://doi.org/10.1002/2015JD024008>, 2016.
760
- 761 Nowell, H., Liu, G., and Honeyager, R.: Modeling the microwave single-scattering properties of
762 aggregate snowflakes, *J. Geophys. Res.: Atmos.*, 118, 7873–7885, <https://doi.org/10.1002/jgrd.50620>,
763 2013.
764
- 765 Padmanabhan, S., Gaier, T. C., Tanner, A. B., Brown, S. T., Lim, B. H., Reising, S. C., Stachnik, R., Bendig,
766 R., and Cofield, R.: TEMPEST-D radiometer: Instrument description and prelaunch calibration, *IEEE*
767 *Trans. Geosci. Remote Sens.*, 59, 10213–10226, <https://doi.org/10.1109/TGRS.2020.3041455>, 2021.
768
- 769 Radhakrishnan, C., Chandrasekar, V., Reising, S. C., and Berg, W.: Rainfall estimation from TEMPEST-D
770 CubeSat observations: A machine-learning approach, *IEEE J. Sel. Top. Appl. Earth Obs. Remote Sens.*,
771 15, 3626–3636, <https://doi.org/10.1109/JSTARS.2022.3170835>, 2022.
772



- 773 Reising, S. C., Gaier, T. C., Padmanabhan, S., Lim, B. H., Heneghan, C., Kummerow, C. D., Berg, W.,
774 Chandrasekar, V., Radhakrishnan, C., Brown, S. T., Carvo, J., and Pallas, M.: An earth venture in-space
775 Technology Demonstration Mission for Temporal Experiment for Storms and Tropical Systems
776 (TEMPEST), in: IGARSS 2018 - 2018 IEEE International Geoscience and Remote Sensing Symposium,
777 Valencia, 6301–6303, <https://doi.org/10.1109/IGARSS.2018.8517330>, 2018.
778
- 779 Ringerud, S., Kulie, M. S., Randel, D. L., Skofronick-Jackson, G. M., and Kummerow, C. D.: Effects of ice
780 particle representation on passive microwave precipitation retrieval in a Bayesian scheme, *IEEE Trans.*
781 *Geosci. Remote Sens.*, 57, 3619–3632, <https://doi.org/10.1109/TGRS.2018.2886063>, 2019.
782
- 783 Rodgers, C. D.: *Inverse Methods for Atmospheric Sounding: Theory and Practice*, World Scientific,
784 Singapore; River Edge, NJ, 238 pp., 2000.
785
- 786 Schmit, T. J., Li, J., Gurka, J. J., Goldberg, M. D., Schrab, K. J., Li, J., and Feltz, W. F.: The GOES-R
787 Advanced Baseline Imager and the continuation of current sounder products, *J. Appl. Meteorol.*
788 *Climatol.*, 47, 2696–2711, <https://doi.org/10.1175/2008JAMC1858.1>, 2008.
789
- 790 Schulte, R. M. and Kummerow, C. D.: An optimal estimation retrieval algorithm for microwave humidity
791 sounding channels with minimal scan position bias, *J. Atmos. Oceanic Technol.*, 36, 409–425,
792 <https://doi.org/10.1175/JTECH-D-18-0133.1>, 2019.
793
- 794 Schulte, R. M., Kummerow, C. D., Berg, W., Reising, S. C., Brown, S. T., Gaier, T. C., Lim, B. H., and
795 Padmanabhan, S.: A passive microwave retrieval algorithm with minimal view-angle bias: Application
796 to the TEMPEST-D CubeSat mission, *J. Atmos. Oceanic Technol.*, 37, 197–210,
797 <https://doi.org/10.1175/JTECH-D-19-0163.1>, 2020.
798
- 799 Siddans, R., Gerber, D., and Miles, G.: *Optimal Estimation Method retrievals with IASI, AMSU and MHS*
800 *measurements: Final Report*, 2015.
801
- 802 Siddans, R.: *Water Vapour Climate Change Initiative (WV_cci) – Phase One, Deliverable 2.2; Version*
803 *1.0*, 2019.
804
- 805 Sun, B., Reale, A., Tilley, F. H., Pettey, M. E., Nalli, N. R., and Barnet, C. D.: Assessment of NUCAPS S-NPP
806 CrIS/ATMS sounding products using reference and conventional radiosonde observations, *IEEE J. Sel.*
807 *Top. Appl. Earth Obs. Remote Sens.*, 10, 2499–2509, <https://doi.org/10.1109/JSTARS.2017.2670504>,
808 2017.
809
- 810 Trent, T., Siddans, R., Kerridge, B., Schröder, M., Scott, N. A., and Remedios, J.: Evaluation of
811 tropospheric water vapour and temperature profiles retrieved from MetOp-A by the Infrared and
812 Microwave Sounding scheme, *Atmos. Meas. Tech.*, 16, 1503–1526, [https://doi.org/10.5194/amt-16-](https://doi.org/10.5194/amt-16-1503-2023)
813 *1503-2023*, 2023.
814
- 815 van de Hulst, H. C.: *Light Scattering by Small Particles*, Wiley, New York, 470 pp., 1957.
816



817 van den Heever, S., Haddad, Z., Tanelli, S., Stephens, G., Posselt, D., Kim, Y., Brown, S., Braun, S., Grant,
818 L., Kollias, P., Luo, Z. J., Mace, G., Marinescu, P., Padmanabhan, S., Partain, P., Petersent, W., Prasanth,
819 S., Rasmussen, K., Reising, S., Schumacher, C., and the INCUS Mission team: The INCUS Mission, in: EGU
820 General Assembly 2022, EGU22-9021, <https://doi.org/doi.org/10.5194/egusphere-egu22-9021>, 2022.